Environmental Research 219 (2023) 115054

Contents lists available at ScienceDirect

Environmental Research

journal homepage: www.elsevier.com/locate/envres

Evaluation of a graphitic porous carbon modified with iron oxides for atrazine environmental remediation in water by adsorption

Cristiane de Oliveira [a], Carmem G. Renda [b], Ailton J. Moreira [c], Otávio A.P. Pereira [a], Ernesto C. Pereira [c], Gian P.G. Freschi [a], Roberto Bertholdo [a,*]

[a] Federal University of Alfenas, Poços de Caldas – MG Campus, Rod. José Aurelio Vilela, BR 267, Km 533, 11999, University City, Zip Code, 37715-400, Poços de Caldas, MG, Brazil
[b] Department of Materials Engineering, Federal University of São Carlos, Rod. Washington Luiz, Km 235, Zip Code, 13565-905, São Carlos, SP, Brazil
[c] Department of Chemistry, Federal University of São Carlos, Rod. Washington Luiz, Km 235, Zip Code, 13565-905, São Carlos, SP, Brazil

ARTICLE INFO

Keywords:
Graphitization. porous carbon. atrazine. adsorption. environmental remediation

ABSTRACT

In the last decades, the growth of world agricultural activity has significantly contributed to the increased presence of emerging pollutants such as atrazine (ATZ) in aquatic ecosystems. Due to its high stability to the natural or artificial degradation processes, the ATZ environmental remediation by adsorption has been investigated. In this study, a graphitic-porous-carbon- (GPC) based material with magnetic domains was applied to remove ATZ from aqueous solution. ATZ high adsorption efficiency in a reduced time was achieved in the presence of the GPC adsorbent, leading to a detailed investigation of the mechanisms involved in the adsorption processes. Pseudo-first-order (PFO), pseudo-second-order (PSO), Ritchie, Elovich, and Weber-Morris models were applied to calculate the kinetic process efficiency. Likewise, adsorption isotherms based on Langmuir, Freundlich, Temkin, and Redlich-Peterson models were applied for a detailed understanding of the adsorption mechanisms. GPC was successfully applied for ATZ remediation in natural waters, confirming its high potential for treating natural waters contaminated by ATZ using adsorption process. The material can also be recovered and reused for up to 4 application cycles due to its magnetic properties, showing that in addition to ATZ adsorption efficiency, its sustainable use can be achieved.

1. Introduction

Atrazine (ATZ) is one of the most used soil-applied pesticides for broadleaf weed control in different agricultural crops (Cougnaud et al., 2005; Jennings and Li, 2017; Švorc et al., 2013). It is easily found in water resources due to its high solubility, low reactivity, and slow degradation by natural processes (Gorito et al., 2017; He et al., 2019). ATZ may cause sexual abnormalities and other problems in aquatic animals as well as present several risks to human health, even at low concentrations (Freeman et al., 2011; Singh et al., 2018). ATZ was banned by the European Union in 2004 (European Commission, 2013) due to the risks associated with its agricultural use. However, its use in countries such as Brazil and the USA, which are world agricultural power-houses is still authorized by their respective federal environmental protection and sanitary control agencies (Brazil, 2005; Ryberg et al., 2020). While ATZ concentrations declined in surface waters in Europe due to it being outlawed, ATZ is often reported as a contaminant of aquatic ecosystems in both USA and Brazil (Barcellos et al., 2022; Karlsson et al., 2020; Ryberg et al., 2020). In USA, ATZ is among the three most detected pesticides in surface water, reaching concentrations of up to 80 μg L^{-1} (Stackpoole et al., 2021). In Brazil, studies have found ATZ concentrations of up to 2.4 μg L^{-1} in surface waters in intra-harvest periods, coinciding with the dates of herbicide application to crops (Buarque et al., 2021). However, ng L^{-1} or μg L^{-1} concentrations detected in surface waters are due to dilution or removal of industrial effluents containing ATZ by other natural processes. In these effluents, reported ATZ concentrations may reach values ranging from 30 to 2153 mg L^{-1}, being sources of pollutant insertion into the aquatic ecosystem that requires special focus (Aquino et al., 2017; Júnior et al., 2021).

Due to its risks to health and the environment, new technologies have been studied for the treatment of water contaminated by ATZ and effluents (He et al., 2019). An example of ATZ degradation technology, heterogeneous photocatalysis and other advanced oxidation processes have been employed (Moreira et al., 2022; Paris et al., 2022). However,

* Corresponding author.
E-mail address: roberto.bertholdo@unifal-mg.edu.br (R. Bertholdo).

https://doi.org/10.1016/j.envres.2022.115054
Received 3 September 2022; Received in revised form 1 December 2022; Accepted 10 December 2022
Available online 12 December 2022

adsorption processes have also stood out in the fast and efficient ATZ removal using low-cost adsorbent materials (Anastopoulos et al., 2020; Cao et al., 2021; Frikha et al., 2022). Porous-carbon-based materials are one of the most viable alternatives for emerging contaminants adsorption (Frikha et al., 2022; Varsha et al., 2022). Obtaining them by different synthesis methods and precursors, such as a carbon source, gives these materials a large surface area, diversified porosity, and high interaction capacity with the absorbed molecules (Jiao et al., 2019; Seibel et al., 2016; Yang et al., 2017). Phenolic resins are potential carbon sources that originate materials with high adsorptive potential physicochemical characteristics when subjected to the ferrocene-catalyzed graphitization process (Renda et al., 2021a; Renda et al., 2021b). Furthermore, the use of ferrocene in this graphitic porous carbon (GPC) synthetic process forms iron oxide in the structure of the material (Renda et al., 2021a; Saeed et al., 2016). Consequently, these iron-oxide-containing carbonaceous materials have magnetic properties, making them even more attractive for water treatment applications due to their potential reuse after recovery by magnetic separation (Batista et al., 2014; Lv et al., 2019; Rahmani-Sani et al., 2020).

The adsorptive removal of ATZ in aqueous solution by porous-carbon-based adsorbents has achieved promising results (>90% in 1 h) for developing new environmental remediation technologies (Jiao et al., 2019; Mandal et al., 2017). These materials feature organic groups, such as –OH, $–CH_3$, $–CH_2$, carbon chains, among others, which interact with the adsorbate by the physio-chemisorption processes (Król et al., 2016; Yang et al., 2017). Also, some of these materials have a complex pore structure that fosters adsorption at superficial or deep adsorbent sites in the material structure (Lawtae and Tangsathitkulchai, 2021; Pinson et al., 2018). Such features of each material allow an adsorbent with a BET surface area (S_{BET} = 1308 m^2/g) to take 23 h longer than an adsorbent with S_{BET} = 192 m^2/g to achieve 90% ATZ adsorption at similar sites (Jiao et al., 2019; Mandal et al., 2017). For a detailed understanding of the adsorption mechanisms involved in organic pollutants removal, kinetic and thermodynamic studies have been conducted (Jaria et al., 2015; Lima et al., 2019; Pelekani and Snoeyink, 2001). Such approach enables concluding whether the adsorption mechanisms involved in each adsorbent-adsorbate interaction are mediated by the surface interactions nature, and pore characteristics, or even influenced by the conditions applied in the experimental assays (Lawtae and Tangsathitkulchai, 2021; Yang et al., 2017).

In considering the risks related to the environmental pollution caused by ATZ and the porous carbon potential to promote efficient environmental remediation, studying new uses of such materials for ATZ treatment by adsorption can contribute to the improvement of the area. Besides, the use of graphitic porous carbon with magnetic domains for ATZ adsorption in simulated effluent and natural waters was studied. Different characterization techniques were applied to reveal the pore nature and the material magnetic potential. ATZ adsorption studies were conducted in detail to find the main kinetic mechanisms involved in ATZ adsorption. Furthermore, adsorption isotherms were applied to comprehend the thermodynamic nature of adsorbent-adsorbate interactions to confirm the material feasibility and applicability on ATZ environmental remediation in aquatic ecosystems. Therefore, its application in water treatment processes and easy reusability may advance the search for sustainable adsorbents on environmental remediation.

2. Experimental

2.1. Polymeric and graphitic porous carbon synthesis (GPC)

Novolak-type phenolic resin was synthesized according to a previous study (Renda et al., 2021a). Phenol (99% purity, Proquimios, Brazil) and formaldehyde (37% w/w, 1.08 g/cm^3 density, Proquimios, Brazil), at a 1:3 phenol: formaldehyde molar ratio, were homogenized by magnetic stirring for 30 min. Hydrochloric acid (37% w/w, Vetec, Brazil) was added to the reaction at a 0:33 formaldehyde: hydrochloric acid molar ratio with magnetic stirring for 90 extra minutes. The mixture featured two phases. The lower phase (resin) was separated and ferrocene was added to the resin at a 3 wt% ratio. The mixture was homogenized for 10 min using an ultrasonic probe (Vertical lab mix plus, 6 kHz), transferred to an alumina crucible, and thermally treated in a tube furnace under reduced argon atmosphere. A 3 °C/min heating rate was applied. The maximum temperature and the respective maintenance time at each level are shown in Table 1.

Table 1
GPC synthetic method heating treatment program.

Level	Initial temperature (°C)	Final temperature (°C)	Maintenance time in final temperature (min)
1	27	80	120
2	80	100	30
3	100	150	30
4	150	200	60
5	200	500	60
6	500	1000	300

In the end of the heating program, the system was naturally cooled to room temperature. The obtained material (GPC) was deagglomerated in an agate mortar, stored, and subjected to characterization analyses and adsorption assays. All synthetic parameters used in the current study were defined in previous studies as an optimized condition to achieve the highest porosity adsorbent (Renda et al., 2019; Renda and Bertholdo, 2018). To identify the experimental flow to obtain GPC, a schematic diagram was shown in Fig. 1.

2.2. GPC characterization

GPC was powdered. The resulting powder was evaluated by powder X-Ray Diffraction (XRD) measurements on a Bruker XRD 8 Advance equipment using CuKα radiation (1.5406 Å) and a 2θ range from 10 to 80° with a = 0.02°/sec step size. The high-resolution transmission electron microscope (HR-TEM) images for the powder were obtained by a Jem-2100 LaB6 (Jeol, Tokyo, Japan) at a 200 kV accelerating voltage coupled to an INCA Energy TEM 200 (Oxford, Abingdon, UK) and Energy Dispersive Spectroscopy (EDS) detector. The samples were ground; the powder solubilized in isopropyl alcohol and dispersed using an ultrasonic dispersion for 30 min. After that, the materials were deposited on copper and carbon grids and dried for 24 h in a desiccator.

Magnetic Field Microscopy (MFM) measurements were performed at room temperature in the air using a non-contact atomic force microscope (NanoObserver, CSInstruments) with a PPP-MFMR-10 (Nanosensor, 45–115 kHz) tip. Initially, the powder was deposited on carbon tape, and the topography with a 5 μm area was scanned at a 0.5 ln/s speed. The tip was elevated by 20 nm, and the sample's DC magnetic field measurements were performed in lift mode. The amplitude and phase images were collected at a 62.37 kHz oscillation frequency, 1.5 V, and a 512 nm resolution. VSM analysis using an EG&G Princeton Applied Research model 4500 magnetometer was used to study the GPC's magnetic property. A 50 Oe/s step ranging from 1000 to −1000 Oe, and 100 Oe/s ranging from 1 k to 10 k Oe and -1 k to −10 k Oe at room temperature were applied on the analysis.

GPC sample porosity was achieved by Nitrogen physisorption using Micromeritics Gemini VII equipment. About 500 mg powder was pretreated at 350 °C under a vacuum atmosphere in a Micromeritics Vap Prep 061 Sample Degas System. Measurements were performed, and gas-phase isotherm physisorption curves were obtained. The specific surface area was obtained using the Brunauer-Emmett-Teller (BET) method for a P/Po ≤ 0.3 range. The GPC sample point of zero charge (PZC) was determined by the eleven points experiment (Regalbuto and Robles, 2004) due mainly to the GPC magnetic characteristic. In this experiment, the different initial pH conditions (1–13) were prepared by dispersing 25 mg GPC in a 25 mL aqueous solution. The pHs were

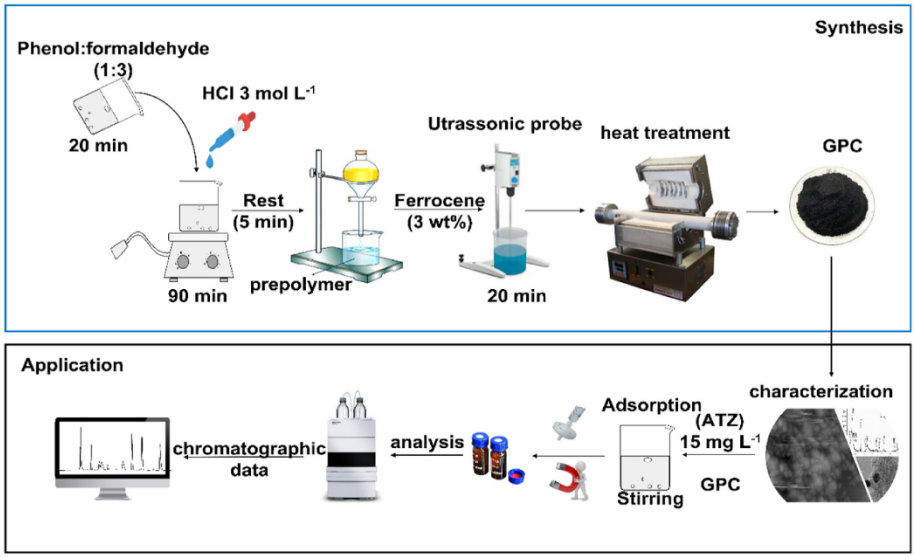

Fig. 1. Diagram of experimental procedures applied in GPC synthesis and Atrazine adsorption assays.

adjusted with HCl and/or NaOH 0.1 mol L $^{-1}$. Such analysis was performed using a pHmeter (827 pHk lab, Metrohm). The initial and final pH were measured at room temperature after 24 h of dynamic contact with the GPC.

2.3. Atrazine adsorption studies

2.3.1. Reagents and solutions

In these studies, a 1000 mg L^{-1}standard atrazine (ATZ) solution (stock) was prepared by dissolving the respective reagent (Sigma-Aldrich, 98%) in HPLC-grade methanol (JT Backer). Ultrapure water (Millipore Milli-Q system, resistivity ≤18.2 MΩ cm) was used to prepare all intermediary solutions. HPLC-grade acetonitrile (JT Backer) was used for the desorption and chromatographic analysis processes.

2.3.2. GPC dosage and initial pH study

To find the optimized ATZ adsorption conditions, GPC suspensions with 200, 300, 400, 500, and 700 mg L^{-1}dosages and different initial ATZ solution pH values were analyzed. The calculated mass for each suspension were added to 20 mL of a 15 mg L $^{-1}$ATZ solution and stirred for 120 min using a Powder Shaker KJ-202. On optimal pH condition, the GPC dosage was set at 500 mg L^{-1}and the contact time at 120 min. ATZ 15 mg L^{-1} solutions had their initial pH values adjusted to 2.2; 5.4; 5.9; 7.9, and 9.7 by adding aliquots of 0.1 mol L^{-1} NaOH or HCl solutions, with pH = 5.4 corresponding to ultrapure water natural pH. After stirring in each sample, the adsorbent was removed from the solution using a 0.22 μm membrane, and the ATZ concentration in the aqueous phase was determined by high-performance liquid chromatography (HPLC – UV, according to the experimental scheme seen in Fig. 1). The optimal GPC dosing conditions and ATZ solution initial pH were defined considering the adsorptive capacity and the adsorption percentage found after analyzing the initial and final ATZ concentrations.

2.3.3. Desorption and recyclability assays

ATZ desorption studies in water or acetonitrile were performed at different times. Firstly, for each study solution, the 5 mg GPC mass was dispersed in 20 mL of a 15 mg L^{-1} ATZ solution and stirred for 120 min to reach adsorption equilibrium. Then, the suspension was centrifuged at 11,000 rpm for 10 min. The phases were separated and the GPC was oven-dried at 50 °C for 1 h. The dried material was transferred to a glass beaker, 10 mL of water or acetonitrile was added (twice), and the mixture was stirred for 2, 5, 10, 15, 20, 40, 60, 90, or 120 min for desorption. At the end of their respective desorption time, the samples were filtered with a 0.22 μm membrane, and the desorbed ATZ concentration was quantified by HPLC.

The recyclability of GPC was analyzed using ATZ adsorption and desorption assays in different application cycles. Thus, 5 mg of GPC was dispersed in 20 mL of 15 mg L^{-1} ATZ solution and stirred at 3000 rpm for 120 min to reach adsorption equilibrium. Afterward, a neodymium magnet was placed near the beaker glass wall for magnetic separation, and the solution was transferred to a centrifuge tube. Centrifugation was used to separate the non-magnetic solids. Next, the solids that had been separated by magnetic attraction and centrifugation were dried at 50 °C for 1 h, and the ATZ concentration was quantified in the supernatant. The material was transferred to a 25 mL beaker, 10 mL (twice) of acetonitrile was added, and the mixture was subjected to desorption for 30 min using an ultrasound bath as extra energy. The phases were then separated aided by a magnet and centrifugation. The supernatant was used to quantify the ATZ concentration after adjusting the volume to 20 mL and the GPC was rinsed twice with water and dried at 70 °C for 1 h for use in the next cycle. Such process was repeated until the material adsorption efficiency was lower than 60% compared to the first cycle.

2.3.4. Adsorption kinetics

To investigate the adsorption kinetic, the 500 mg L^{-1} GPC dosage, the 20 mL 15 mg L $^{-1}$ ATZ solution at pH = 5.4, and 25 ± 1 °C temperature were fixed. The time study ranged from 5 to 120 min under constant stirring. After each adsorption period, the solutions were filtered, and the ATZ concentration quantified by HPLC. The assays were performed in triplicate, and the adsorption capacity at equilibrium time (q_e) was determined using Equation (1) [40].

$$amount\ adsorbed\ (q_e) = \frac{(C_0 - C_e)}{m} V \quad (1)$$

where C_0 is initial ATZ concentration in the liquid phase (mg L^{-1}), C_e is ATZ concentration in the liquid phase at equilibrium (mg L^{-1}), V is volume of suspension (L) and m is adsorbent mass (g). The fit to the adsorption no-linear kinetic model of pseudo-first-order (PFO, Equation (2)) and pseudo-second-order (PSO, Equation (3)) and Elovich (Equation (4)), and Ritchie (Equation (5)) were studied (Li et al., 2021; Peiravi-Rivash et al., 2022).

$$q_t = q_{e1}\left[1 - exp^{(-K_1.t)}\right] \quad \text{PFO model} \quad (2)$$

$$q_t = \frac{q_{e2}^2.K_2.t}{[K_2.(q_{e2}).t + 1]} \quad \text{PSO model} \quad (3)$$

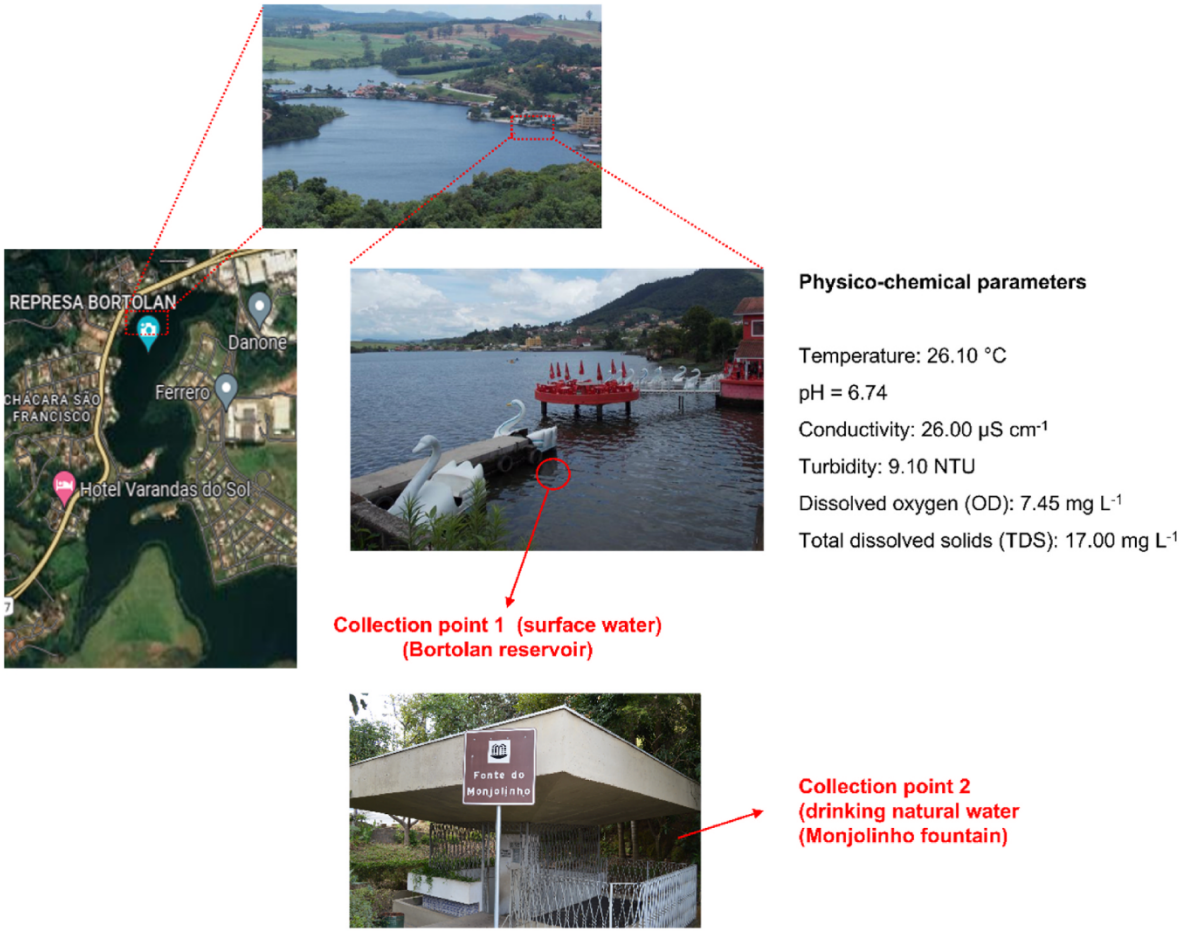

Fig. 2. Collection points identification from a surface or natural water sources.

$$q_t = \frac{1}{\beta}[\ln(1+\alpha\beta t)] \text{ Elovich model} \quad (4)$$

$$q_t = \frac{q_e.K_R.t}{1+K_R.t} \text{ Ritchie model} \quad (5)$$

Where K_1 is PFO kinetic constant (min^{-1}), K_2 is PSO kinetic constant (mg g^{-1} min^{-1}), q_e is equilibrium adsorption capacity (mg g^{-1}), and q_t is adsorptive capacity of material at time t (minutes), K_R is the constants of Ritchie (min^{-1}), α and β are the initial rate constant (mg g^{-1} min^{-1}) and desorption constant (mg g^{-1}) in Elovich model, respectively. The fit to the models was verified from R^2 and of the χ^2 and Δq (%) statistical indices which was calculated from equations (6) and (7).

$$\chi^2 = \sum_{i=1}^{N}\left(\frac{(q_{e,exp.} - q_{e,cal.})^2}{q_{e,cal.}}\right) \quad (6)$$

$$\Delta q(\%) = 100\sqrt{\frac{1}{N-1}\sum_{i=1}^{N}\left(\frac{q_{exp}-q_{cal}}{q_{exp}}\right)_i^2} \quad (7)$$

where, and, $q_{e,exp}$ is the experimental adsorption capacity (mg g^{-1}), and $q_{e,\,cal.}$ Is the calculated adsorption capacity (mg g^{-1}) by the adjustments of each kinetic model studied.

2.3.5. Adsorption isotherms and thermodynamic parameters

The adsorption equilibrium isotherms were obtained at 30, 40, and 50 °C using ATZ solutions at different concentrations (0.5; 2; 5; 50; 75, 100, 150, 200 and 250 mg L^{-1}), pH = 5.46 and a fixed 500 mg L $^{-1}$GPC dosage. The adsorption assays were carried out at 150 rpm stirring for 120 min using a Dubnoff bath (Bunker®, model NI 1232). After equilibration, the solutions were filtered with a 0.22 µm membrane, and the ATZ concentration in the aqueous phase was determined by HPLC. The assays were performed in triplicate, and the adsorption capacity at equilibrium time (q e) was determined according to Equation (1). The obtained curves were correlated with the Langmuir, Freundlich, Temkin, and Redlich-Peterson models to determine the parameters of the isotherms.

The Langmuir (Eq. (8)), Freundlich (Eq. (9)), Redlich-Peterson (Eq. (10)), and Temkin (Eq. (11)) nonlinear equations equation were used to calculate the physical-chemical parameters required to understand the adsorption mechanism (Lima et al., 2019; Saxena et al., 2019; Tran et al., 2017).

$$q_e = \frac{Q^0_{max}\,K_L C_e}{1+K_L C_e} \quad (8)$$

$$q_e = K_F\,C_e^{1/n} \quad (9)$$

$$q_e = \frac{K_{RP}\,C_e}{1+a_{RP}\,C_e^g} \quad (10)$$

$$q_e = \frac{RT}{b}[\ln(K_T Ce)] \quad (11)$$

Where Q°_{max} (mg g^{-1}) is maximum adsorption capacity of an adsorbent, C_e (mg L^{-1}) is adsorbate concentration at equilibrium, q_e (mg g^{-1}) is the amount of adsorbate uptake at equilibrium, and K_L (L mg^{-1}) is a constant of affinity between an adsorbent and adsorbate, K_F is Freundlich constant ($mg^{1-(1/n)}$. $L^{1/n}/g$), n is heterogeneity factor, K_T (L g^{-1}) is

Table 2
Samples identification refers to the adsorption processes in natural water. In these assays, 5 mg GPC, 20 mL solution, and a 120-min contact were fixed.

Sample	$[ATZ]_O$ (mg L^{-1})[a]	Adsorbent
Monj_0 or Bort_0	–	Natural[b]
Monj_1 or Bort_1	15	GPC
Monj_2 or Bort_2	15	Natural

[a] Initial ATZ concentration.
[b] Solids present in natural waters.

theequilibrium binding constant corresponding to the maximum binding energy, b (kJ mol^{-1} L^{-1}) is the adsorption heat of surface and B is the Temkinconstant related to the heat of adsorption (B = RT/b), R is ideal gas constant, and T is temperature in Kelvin (K), K_{RP} (L g^{-1}) and a_{RP} (mg $L^{-1})^{-g}$ are the Redlich-Peterson constants and g (dimensionless) is an exponent whose value must range between 0 and 1. The thermodynamic behavior of the adsorption was verified by the Gibbs free energy (ΔG, kJ mol^{-1}) variation, calculated using Equations (12) and (13), respectively (Lima et al., 2019; Tran et al., 2017).

$$K_e = \frac{K_L * 1000 * MM_{ATZ} * [ATZ]^{\circ}}{\gamma} \quad (12)$$

$$\Delta G^{\circ} = -RTln(K_e) \quad (13)$$

Where K_e is equilibrium constant (dimensionless), MM_{ATZ} is molar mass of adsorbate (215.68 g/mol, atrazine), K_L is equilibrium constant obtained by equation (8)(best fit model), $[ATZ]^{\circ}$ is the standard concentration of the adsorbate (1 mol L^{-1}), γ is the coefficient of activity (dimensionless) T is absolute temperature (K), and R is gas constant, and ΔG° is Gibbs energy expressed in kJ mol^{-1}. According to the literature, for dilute solutions the γ can be considered unitary (Lima et al., 2019).

2.3.6. GPC application in natural water

Adsorption studies with natural water were conducted using sample collected from the Bortolan reservoir, located in Poços de Caldas, MG, Brazil (−21.781219, −46.636225). The collection point and water quality parameters were measured *in situ* using a Multi Water Quality Checker (Horiba, U-50 Series) and can be seen in Fig. 2. The second natural water sample was collected at the Monjolinho spring located in the same city (−21.79296, −46.55652).

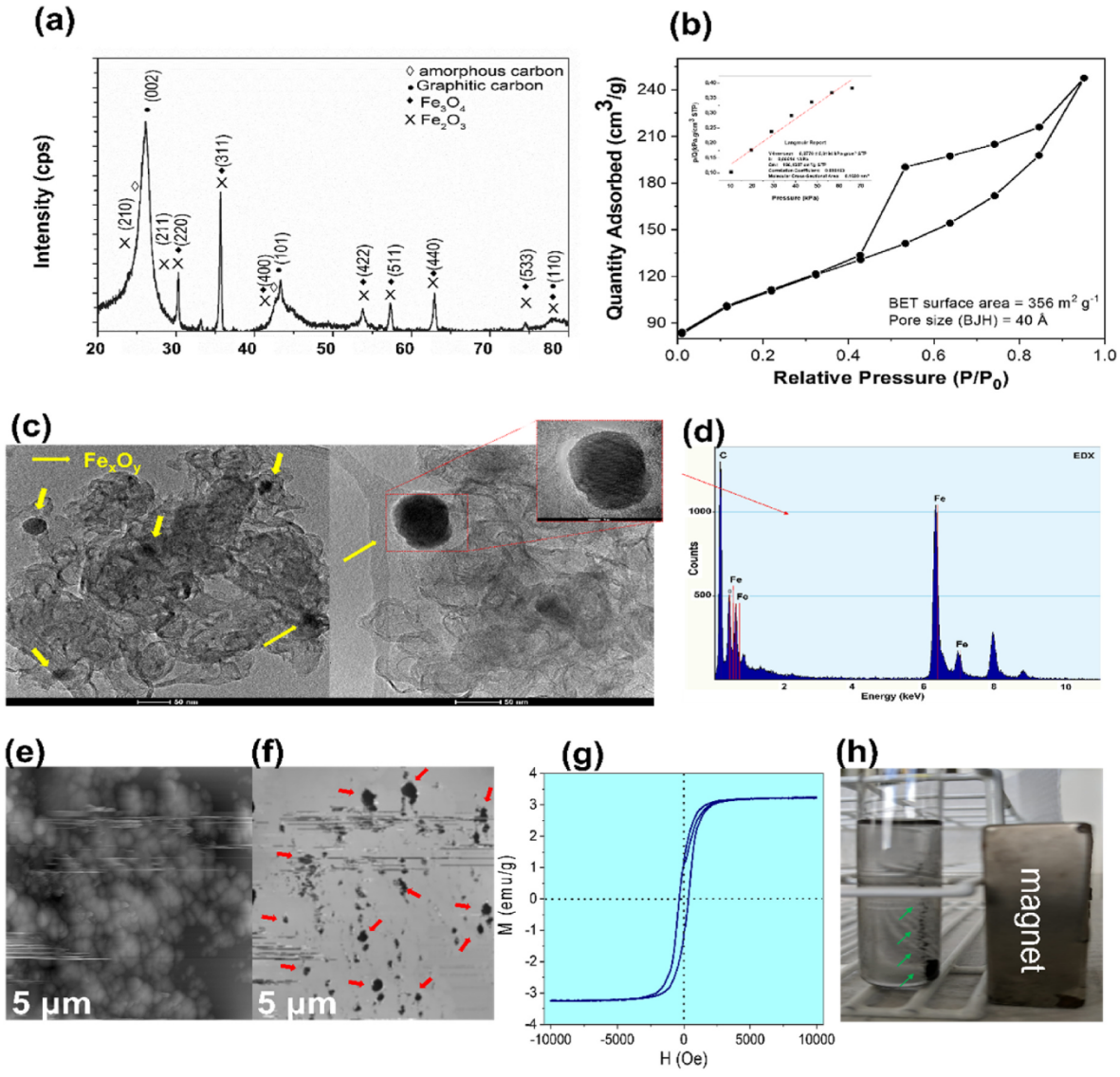

Fig. 3. XRD pattern (a), Nitrogen physisorption hysteresis (b) HR-TEM image (c), EDX spectrum (d), topography (e), magnetic domain (f) image by MFM, and VSM analyses (g). Magnetic attraction by neodymium magnet (h).

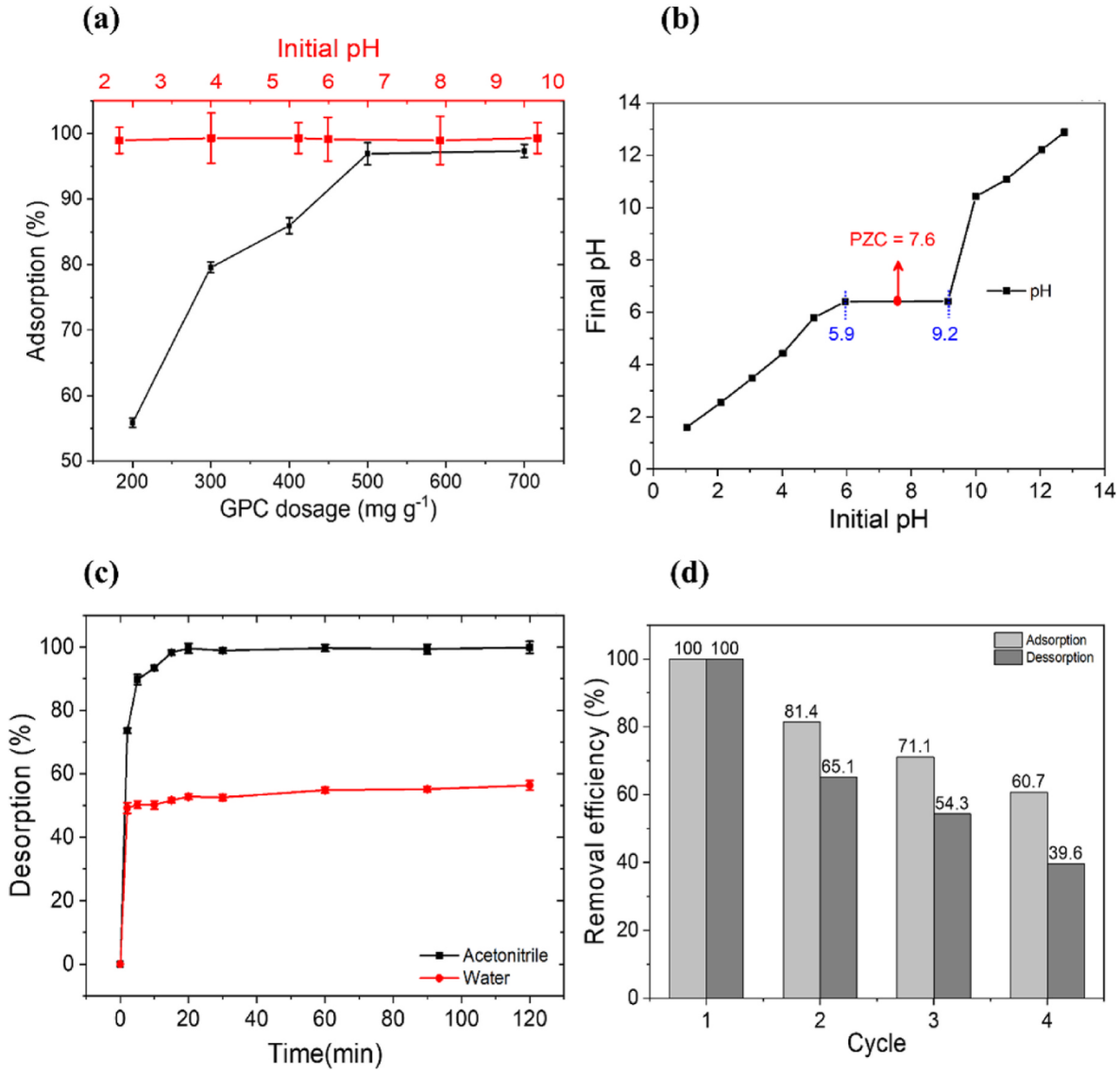

Fig. 4. ATZ adsorption optimization as a function of GPC dose (mg L^{-1}) or initial pH (a), potential of zero charge (PZC) measurements at different pH (b), desorption assays in water or acetonitrile (c), and material reuse (d).

The physicochemical features of this second matrix were compatible with the quality of water used for human consumption according to the Brazilian sanitary legislation (Brazil, 2005). For the solutions prepared with natural water, amounts of ATZ stock solution (1000 mg L^{-1}) were diluted in this matrix to obtain a final ATZ 15 mg L^{-1} solution. The 5 mg GPC mass was added to 20 mL of this solution, the adsorption time was set at 120 min, and the solution was filtered through a 0.22 μm membrane to remove solids. The samples corresponding to the Monjolinho spring or Bortolan reservoir were identified as Monj or Bort, respectively. For clarity, Table 2 identified the adsorption processes in natural water.

ATZ quantification was performed using high-performance liquid chromatography with a UV–Vis detector (221 nm). Equipment details, chromatographic conditions, and figures of merit corresponding to the analytical method were presented in a previous study (Moreira et al., 2021).

3. Results and discussion

3.1. GPC characterization

XRD pattern (Fig. 3a) showed that the GPC structural composition consists mainly of graphitic carbon and iron oxide, indexed by crystallographic planes (002), (101), (110), and (220), (422), (511), (440) of greater intensity, respectively (Li et al., 2007; Paris et al., 2022; C.G. Renda et al., 2021). In addition to the overlap observed near 42.5°, amorphous carbon was identified to a lesser extent in the shoulder shape at 24° in the broad-based diffraction peak at the 20 to 30° region. GPC structural nature was compatible with the materials synthesized in a previous study using similar synthesis parameters to obtain a graphitic composite with iron sites and high porosity (Renda et al., 2021a; Renda et al., 2021b).

The graphic profile observed in Fig. 3b fitted into H2-type hysteresis, that is a feature of materials with complex structures where pore size distribution and shape are not well-defined (Alothman, 2012). The adsorption-desorption kinetics got a good fit by the Langmuir model ($R^2 = 0.98$), allowing for a reliable GPC porosity characteristics calculation. BET surface area (S_{BET}) and pore sizes were $S_{BET} = 358\ m^2\ g^{-1}$ and 40 Å,

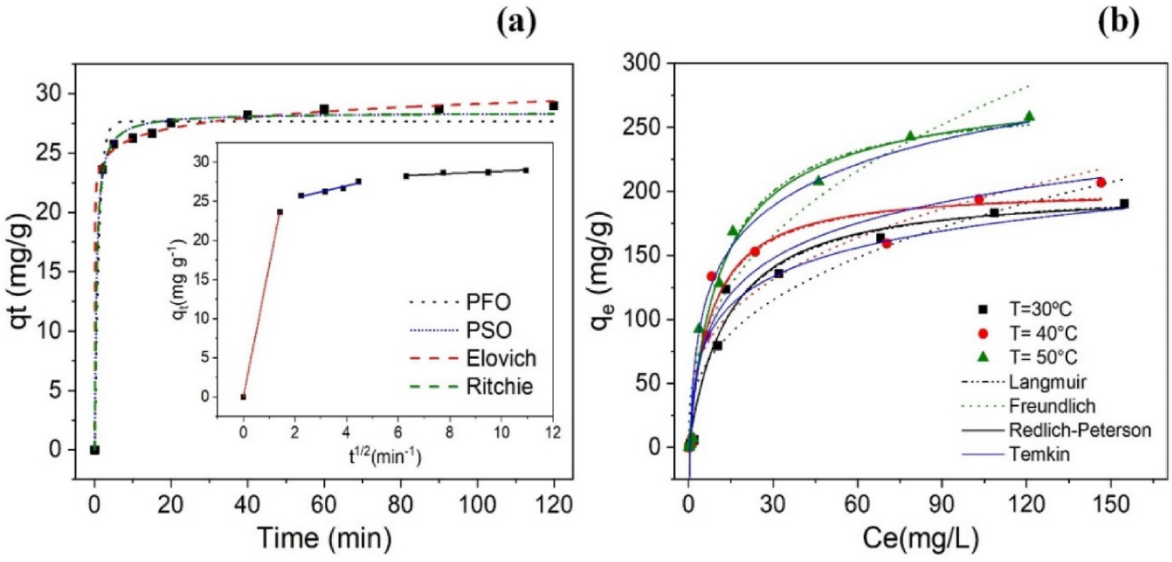

Fig. 5. ATZ kinetic study with Weber and Morris model insert (a) and adsorption isotherms (b).

respectively, confirming GPC high surface area and porosity. Besides, the calculated micropore volume ($V_{\mu pore}$) was $V_{\mu pore} = 0.248$ cm^3 g^{-1}, indicating the potential of GPC how adsorbent. HR-TEM image (Fig. 3c) showed the graphitic structure as the main GPC component, and some higher-density spheres, corresponding to iron oxide, were identified in different surface regions (indicated by yellow arrows). EDX analyses (Fig. 3d) performed precisely under the spheres confirmed Fe as the main component, in addition to oxygen and carbon. These results demonstrated that Fe-modified porous carbon production was successfully achieved using the method proposed by Renda et al. (Renda et al., 2021a; Renda et al., 2019).

GPC magnetic domain regions formed by the presence of iron oxide in its structure were analyzed by MFM. The material was deposited on the substrate as agglomerates, where the contours recovered by scanning in non-contact mode showed a spherical morphology topography (Fig. 3e). The topography was composed of phases identified by different grayscale shades. The darker gray areas corresponded to higher density regions that may be due to greater graphitic carbon agglomeration or the presence of randomly distributed iron oxide particles, as shown in the HR-TEM images (Fig. 3b). After topographic mapping, Fig. 3f showed different magnetic domains regions (indicated by red arrows) resulting from the interaction between the tip and the magnetic iron oxide. When the tip interacts with the material magnetic domains, the magnetic image achieves a more intense contrast, highlighting the random distribution of magnetic domains in the material (Batista et al., 2014). Fig. 3g showed the magnetization curve obtained for the GPC sample measured in a magnetometer ranging from 10 to −10 KOe at room temperature. The curve "S" profile is characteristic of ferromagnetic materials, confirming that iron oxide distributed in the adsorbent induced the magnetic domains as shown in the MFM analysis (Fig. 3f) (Batista et al., 2014; Hong et al., 2022; Li et al., 2016). From the higher fields extrapolation, the calculated saturation magnetization value was 3.2 emu/g, and the magnetic hysteresis loop verified under a varying magnetic field application confirmed the material good response to the magnetic stimulus (Li et al., 2016). Such results corroborate with the random iron oxide distribution observed in the HR-TEM images, indicating the magnetic property dependency in relation to iron oxide which is a by-product of the graphitization reaction.

The magnetic material potential was tested by dispersing the powder in water, followed by approaching a neodymium magnet. As indicated in Fig. 3h (green arrows), material accumulation was observed on the test tube wall near the magnet due to magnetic attraction. However, the material's magnetic intensity was limited to the iron oxide regions, resulting in the dispersion of a material portion. It is worth noting that the method used to obtain GPC applies ferrocene as a catalyst in the phenolic resin graphitization process, with iron oxide as its by-product (Renda et al., 2021a). Thus, the magnetic property is a complementary feature for this high-porosity material that may benefit studies where reuse is relevant, especially for pollutant removal from aqueous media (Ahsan et al., 2019; Zielińska-Jurek et al., 2017).

3.2. ATZ adsorption assays

GPC adsorptive capacity was analyzed using ATZ solutions (15 mg L^{-1}) under different experimental conditions. Fig. 4a showed that by increasing the GPC dosage from 200 to 500 mg L^{-1} the ATZ removal efficiency increased by up to 41%. This greater efficiency is due to mechanisms mediated by physisorption processes between ATZ and GPC, in which electrostatic interactions such as π-anion, carbon-hydrogen, hydrogen bonds, and others stand out (Mandal et al., 2021). Fig. 1a showed that GPC is composed of graphitic and amorphous carbon. At the same time, more specific characterization analyses performed in a previous study, such as ^{13}C-NMR, identified numerous functional groups responsible for such interactions (Renda et al., 2021). At doses greater than 500 mg L^{-1}, the ATZ removal efficiency remained at 97 ± 1%, reaching $q_e = 29.2 \pm 1.7$ mg g^{-1}, being the amount of pesticide remaining in the solution (~3%) result of equilibrium between adsorption-desorption. Therefore, the 500 mg L^{-1} dose was enough to efficiently remove ATZ from the aqueous solution. By fixing the dose at 500 mg L^{-1} and varying the solution pH from 2.2 to 9.7, ATZ removal was constant for a high-efficiency level (>97%). These results indicated that the reaction medium pH does not affect the GPC surface characteristics, keeping its adsorption sites active under acidic or basic conditions.

With intention to study the impact of pH on GPC surface charge, PZC was determined by the eleven points experiment (Fig. 4b) combined with the final pH monitoring after GPC stirring in the solution. The results showed that the solution final pH did not show any significant changes between pH = 5.9 at 9.2, and the PZC was 7.6. Such result is a promising one, showing the material potential use as an adsorbent for atrazine at natural pH. However, this surface charge did not result from effective bonds but from electrostatic interactions (Lv et al., 2019; Zhu et al., 2015). Such dynamic in interacting with (+) or (−) charges may be due to the carbon groups' diversity as mentioned previously,

Table 3
Atrazine adsorption kinetic parameters.

PFO model		PSO model	
q_e^1 (mg g^{-1})	27.7 ± 0.40	q_e^2 (mg g^{-1})	28.4 ± 0.27
k_1 (min^{-1})	0.93 ± 0.14	k_2 x 10^3 (g mg^{-1} min^{-1})	76.7 ± 12.0
R^2	0.984	R^2	0.995
χ^2	0.153	χ^2	0.020
Δq (%)	4.12	Δq (%)	1.51
Elovich model		**Ritchie model**	
α (mg $g^{-1}min^{-1}$)	1.23 × 10^8	q_e (mg g^{-1})	28.4 ± 0.27
β (mg g^{-1})	0.789	K_R (min^{-1})	2.18 ± 0.33
R^2	0.998	R^2	0.995
χ^2	0.012	χ^2	0.020
Δq (%)	1.19	Δq (%)	1.51
Weber and Morris model			
Linear region	**k_{WB} (mg g^{-1} $t^{-1/2}$)**	**C**	**R^2**
(I)	-	-	-
(II)	0.76 ± 0.14	23.9 ± 0.49	0.905
(III)	0.15 ± 0.04	27.3 ± 0.36	0.810

resulting in high ATZ removal efficiency. ATZ desorption was also tested in the presence of water and acetonitrile at different times (Fig. 4c), reaching desorption values of 49 ± 2% in water and 73 ± 1% in ACN at 2 min. Upon increasing the time to 120 min, ATZ achieved 56 ± 2% desorption in water compared to 100 ± 2% desorption in ACN at 20 min, which was kept until reaching 120 min.

ATZ efficient desorption in the presence of ACN was due to the pesticide's greater solubility in less polar solvents (Jia et al., 2013). The desorption process was irreversible for 44% of the adsorbed molecules in the presence of water. Such results were relevant as they indicated that after the adsorption process, ATZ may be efficiently desorbed in ACN for GPC reuse. Then, the recyclability of GPC in up to 4 application cycles was studied, and shown Fig. 4d. In the first cycle, adsorption reached its maximum value (100%), which gradually decreased to 60.7%, while desorption) was 100% at 39.6% in the fourth cycle. Some experimental procedure aspects adopted in this study may have contributed to efficiency decrease over the application cycles. The first aspect is related to possible material loss in the recovery step, processed by magnetic attraction followed by centrifugation. The process is affected by the lost material in the recuperation decreasing dosage 500 mg L^{-1} dosage that was first established. The second aspect is associated to the material treatment at low temperatures and drying time (50 °C and 1 h, respectively) after desorption. Such conditions may not have been enough to eliminate any residual water and activated the adsorbent sites, affecting the efficiency after each application cycle. Increasing the temperature and drying time could reactivate these adsorption sites with more efficiency and, therefore, such conditions should be covered in future studies. The third aspect is related to the variety of adsorptive mechanisms dominated by different kinetic and thermodynamic processes discussed in sequence.

3.3. Adsorption kinetic and isotherms

Fig. 5 and Table 3 showed the graphic profile and fitting parameters for all the kinetic models calculated from the amounts (q_t) of ATZ adsorbed *versus* time (min). After only 5 min, GPC reached 82% of ATZ maximum adsorption capacity (q_t = 28.9 ± 0.16 mg g^{-1}), while q_t average variation (from 5 min) was only 3% up to 120 min. ATZ adsorption kinetic parameters shown in Table 3 confirmed the best fits were obtained for PSO (R^2 = 0.995), Ritchie (R^2 = 0.995), and Elovich (R^2 = 0.998). On the other hand, the adjustment for PFO was slightly lower (R^2 = 0.984). As the PFO model disregards the interaction between adsorbent and adsorbate as a mechanism controlling the adsorption rate, the worst fit suggests that this mechanism is not the main one for ATZ and GPC. However, the good fits observed for the PSO and Ritchie models corroborated with the high surface areas and

Table 4
ATZ adsorption equilibrium parameters in GPC at different temperatures.

Model	Temperature (°C)		
	30	40	50
Langmuir			
Q°_{max} (mg g^{-1})	204.8	204.7	275.4
K_L (L mg^{-1})	0.071	0.127	0.088
R^2	0.97	0.94	0.98
χ^2	0.68	4.26	1.46
Δq (%)	4.01	9.76	5.01
Freundlich			
K_F ($mg^{1-(1/n)}.L^{1/n}/g$)	33.3	44.5	45.1
n	2.74	3.14	2.62
R^2	0.91	0.86	0.92
χ^2	4.56	9.47	14.9
Δq (%)	9.65	13.0	15.0
Tempkin			
k_T (L g^{-1})	2.07	1.37	1.84
b (kJ mol^{-1} L^{-1})	77.9	65.4	57.1
R^2	0.94	0.95	0.97
χ^2	0.52	4.45	1.07
Δq (%)	3.05	9.95	4.23
Redlich-Peterson			
K_{RP} (L g^{-1})	14.0	25.4	26.2
a_{RP} (mg L^{-1})$^{-g}$	0.065	0.117	0.112
g	1.02	1.01	0.96
R^2	0.97	0.94	0.98
χ^2	0.82	4.72	1.58
Δq (%)	4.26	10.5	5.26

presence of organic groups that denote a lot of active sites in GPC. Just as the PSO and Ritchie models assume that the adsorption mechanism is due to the presence of active sites, the good fit observed for the Elovich model also confirms that the activation energy increases due to the heterogeneous surface of the adsorbent. The statistical indice χ^2 and Δq (%) assumes values closer to zero when experimental data are closer to theoretical data (Mohammadzadeh et al., 2022). Therefore, the low values of χ2 and Δq (%) obtained for the PSO, Elovich and Ritchie models compared to the highest value of χ^2 and Δq (%) observed for PFO, confirm that the adsorption kinetics of ATZ by GPC follows a surface interaction mechanism by active sites.

The experimental adsorption capacity ($q_{e,\ exp.}$) for each time from 40 min is very close to the values obtained by fitting the PSO, Elovich and Ritchie models. Therefore, it is possible to affirm that the adsorption kinetic of ATZ by GPC, occurs by external and internal mass transfer mechanisms in active sites (Naushad et al., 2019; Vargas et al., 2011; Zhu et al., 2015). The α magnitude calculated from the Elovich equation showed that the initial adsorption rate is very high, achieving ATZ surface coverage fast and efficiently by the adsorption. The low value of β confirms that desorption is a non-preferential process, maintaining the ATZ adsorbed in active sites. Thus, Elovich equation parameters show that GPC has highly active sites spread across its surface and R^2 = 0.998 confirmed the optimal fit to the model. As the GPC surface is covered by the ATZ, the adsorption rates decrease because the molecules need to adsorb to non-surface (intra-particle) sites, which occurs more slowly until reaching equilibrium. The Weber and Morris model was applied to describe the intra-particle diffusion mechanisms involved in ATZ adsorption process (Sun and Yang, 2003). Fig. 5 (insert) showed the q_t versus $t^{1/2}$ curve divided into three linear regions (I, II, and III), while the parameters k_{WB}, C, and R^2 were shown in Table 3. As the adsorption kinetics was very efficient after 5 min, the number of points for this interval was not enough to obtain k_{WB}, C, and R^2 values in region I. However, the high slope observed in region I was characterized by an external adsorption domain mediated by surface interaction between adsorbent and adsorbate (Sun and Yang, 2003; Wang et al., 2022), corroborating with the observations discussed from the kinetic models. N_2 physisorption assays (Fig. 3b) showed a high surface area (358 m^2 g^{-1}) and a 40 Å pore size for GPC. As ATZ had a size and depth of 9.6 and 8.4 Å (Pelekani and Snoeyink, 2001), respectively, the pesticide easily

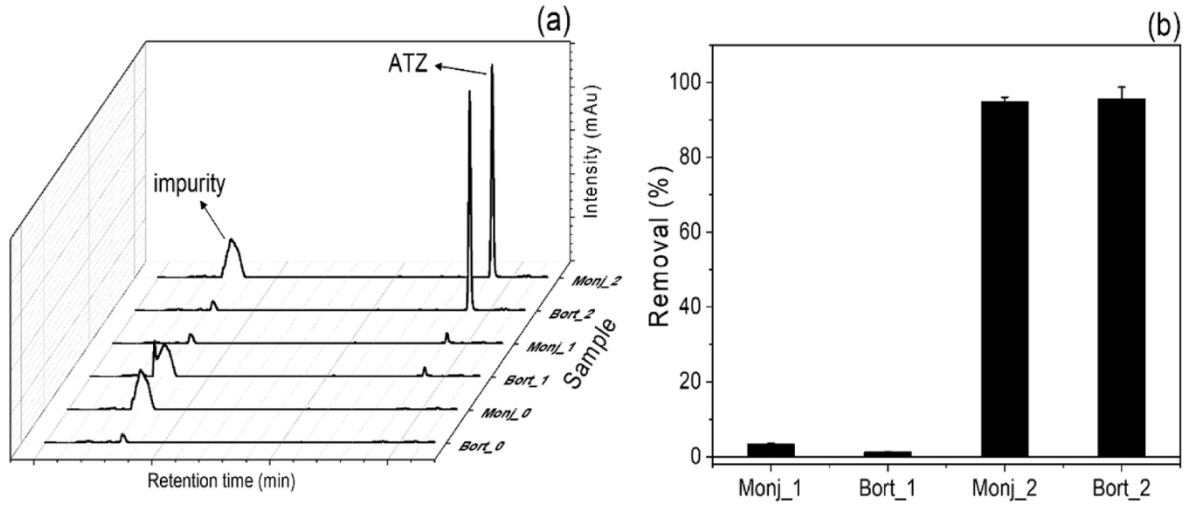

Fig. 6. ATZ chromatograms (a) and adsorption efficiency (b) in natural waters.

percolated through the GPC pores and remains effectively adsorbed by physisorption mechanisms on the material surface. GPC porosity allowed adsorptions to occur in an internal intra-particle environment represented by linear region II with $k_{WB} = 0.76$ mg g^{-1} $t^{1/2}$, which also indicated strong initial adsorption in this environment (Wu et al., 2009). However, as the adsorption process reached an equilibrium between regions II and III, a slight values variation next to region III resulted in a reasonable linear fit ($R^2 = 0.905$). The few non-adsorbed molecules diffused into the macropores to find free adsorption sites. However, the diffusion rate was limited by the low ATZ concentration remaining in the solution and by the counter-diffusion mechanism that leads to adsorption-desorption equilibrium. This final process was observed in linear region III, which showed the lowest $k_{WB} = 0.15$ mg g^{-1} $t^{1/2}$ and $R^2 = 0.810$ values, while the high and positive values found for parameter C justified an initial fast adsorption, and the poor fit linear in this region.

ATZ adsorption isotherms and equilibrium parameters that were calculated by fitting Langmuir, Freundlich, Temkin, and Redlich-Peterson models at 30, 40, and 50 °C are presented in Fig. 5b and Table 4. Comparing the Langmuir and Freundlich models, R^2 average value at the three temperatures was $R^2 = 0.96 \pm 0.02$ for Langmuir and $R^2 = 0.90 \pm 0.03$ for Freundlich, respectively. The good fit found for the Langmuir model confirmed that ATZ adsorption efficiency on GPC occurred with the formation of the monolayer during the first few minutes of process. These results corroborate the good fit for the PSO kinetic parameter and Elovich presented above. The Langmuir model best fitted the experimental data as it showed the highest a R^2 average value, indicating the adsorption mechanism action on the monolayer (Blázquez et al., 2010; Vargas et al., 2011). As GPC has a high surface area, the Temkin model was applied to analyze the nature of interaction between the adsorbate, and the adsorbent surface. The results showed a good fit for all three temperatures ($R^2 = 0.96 \pm 0.02$), confirming the adsorption mechanism consistency over a heterogeneous surface, where the adsorption energy, represented by the parameter *b*, decreases linearly as the coating increases. (Hu and Zhang, 2019). This behavior observed by the good fit to the Temkin model corroborates the results obtained by the PSO, Ritchie, and Elovich models.

The Redlich-Peterson model combined the Langmuir and Freundlich models in a single equation (Tran et al., 2017). Next, it was applied as an important complement to establish the correct model involved in ATZ adsorption by GPC. The fit was also considered good ($R^2 = 0.963 + 0.02$) and similar to that obtained in the Langmuir model. The Redlich-Peterson model compatibility with the Langmuir one was also confirmed by the g values, which was $g = 0.997 \pm 0.032$ for the average of three temperatures, in addition to an $a_{RD} < 1.0$ value (Tran et al., 2017). Curves q_e versus C_e (Fig. 5b) are characteristic of Type I isotherms indicating the prevalence of adsorption processes mediated by micro or mesoporous materials (Achari et al., 2021; Lawtae and Tangsathitkulchai, 2021). The curves profile at all temperatures confirms an adsorption process favorable to high adsorbate mass retention over the adsorbent mass. Such mechanism shows that adsorption equilibrium was reached under low final adsorbate concentrations in the solution (Lawtae and Tangsathitkulchai, 2021).

The Langmuir model also showed that the increase in temperature improved the adsorption capacity at equilibrium, resulting in an increase from $q_e = 204.8$ mg g^{-1} at 30 °C to 275.4 mg g^{-1} at 50 °C. Such results indicate that ATZ adsorption on GPC was actively favorable. As in the kinetic study, the good fits obtained for the Langmuir, Temkin, and Redlich-Peterson models do not allow concluding what best represents the ATZ adsorption processes in GPC. Therefore, the χ^2 and Δq (%) statistical indices were calculated for all isotherm models studied. No significant variation for the calculated statistical indices was noticed when applying the Langmuir, Temkin, or Redlich-Peterson models. This correspondence between the values is because these three models are applied to explain adsorption processes by similar mechanisms. However, a greater deviation and distance from zero were verified for the tests conducted at a temperature of 40 °C for the Langmuir, Temkin, and Redlich-Peterson models. Only for the Freundlich model did the statistical indices distance themselves more significantly from zero, confirming that this model does not explain the ATZ adsorption processes in GPC.

From equations (12) and (13), the calculated $\Delta G = -24.3$ kJ mol^{-1} at 30 °C, $\Delta G = -26{,}6$ kJ mol^{-1} at 40 °C, and $\Delta G = -26{,}4$ kJ mol^{-1} at 50 °C confirm that the adsorption process of ATZ on GPC is thermodynamically favorable and occurs spontaneously, corroborating other studies in the literature (Cheng et al., 2022; Lazarotto et al., 2022).

3.4. ATZ adsorption on real samples

Fig. 6 showed the results of ATZ removal in natural water samples collected from a reservoir (Bortolan) and a natural drinking water source (Monjolinho spring) applying GPC under optimized adsorption conditions. Fig. 6a showed that the chromatograms obtained for the water matrices not fortified with ATZ (Monj_0 and Bort_0) did not show any associated peaks to the pesticide. Matrices fortified with ATZ and submitted to the GPC adsorption process (Monj_1 and Bort_1), showed chromatograms from the final solution analysis confirming an ATZ removal >95%. This removal efficiency in natural waters was compatible with the values obtained in the adsorption studies in ultrapure water (Fig. 4).

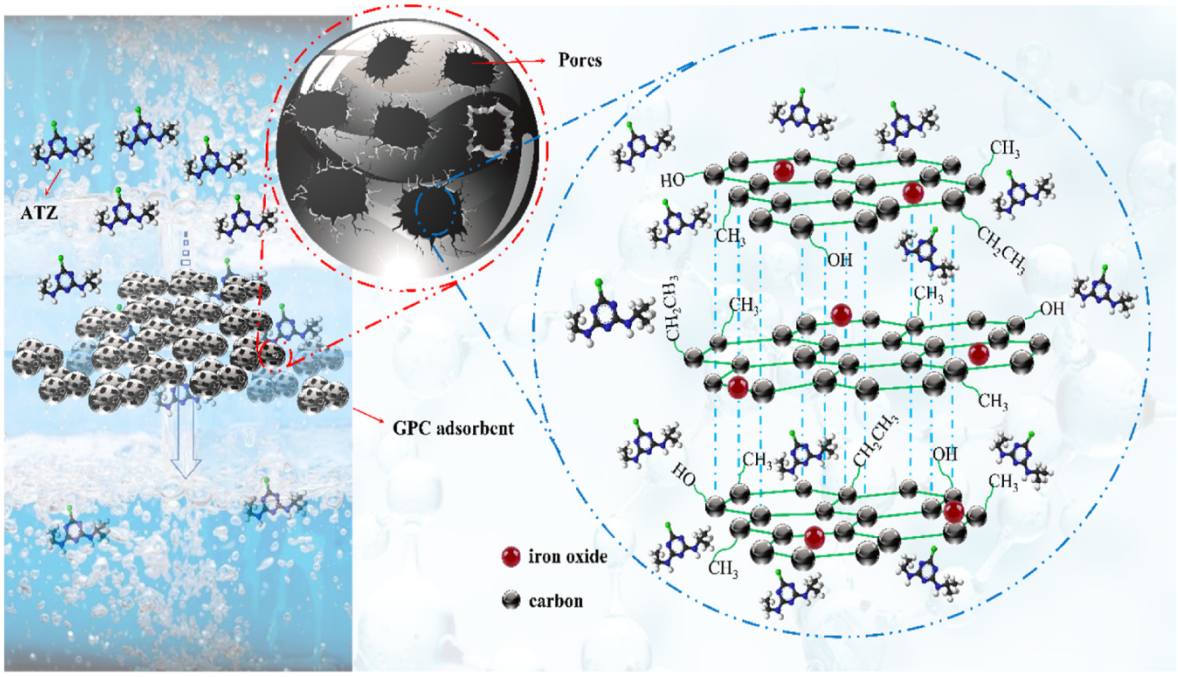

Fig. 7. A proposed mechanism for ATZ adsorption by GPC.

Table 5
Comparative efficiency data for ATZ removal by adsorption using different adsorbent materials.

Material	Adsorbent dosage (mg L^{-1})/sample volume (mL)/ ATZ (mg L^{-1})	BET área (m^2 g^{-1})	q_m (mg g^{-1})	Removal (%)/Time (h)	Reference
N-doped porous carbon sheets	375/40/35	1067	268	87/80	Yang et al. (2017)
Biochar	333/30/10	192	–	90/1	Mandal et al. (2017)
Biochar	1000/10/10	192	–	58.9/24	Mandal et al. (2021)
Biochar	1500/20/5	98	3.44	–	Hernandes et al. (2022)
Porous Graphitic Biomass Carbons	100/100/10	1308	180	90/24	Jiao et al. (2019)
Biochar	2000/10/10	9.21	2.7	–	Sbizzaro et al. (2021)
N-doped biochars	25/100/5	700	103.6	–	Cheng et al. (2022)
activated carbon	1000/50/20	431	55.87	–	Lazarotto et al. (2022)
activated carbon of kaki fruit waste	1000/25/150	1067	211.5	100/60	Salomón et al. (2022)
Graphitic porous carbon (GPC)	500/20/15	358	275.4	>95%/ 0.33	This work

The results for samples Monj_2 and Bort_2, representing natural adsorption processes, showed the matrices were not able to remove ATZ without GPC. ATZ removal efficiency in the absence and presence of GPC is shown in Fig. 6b. The results led to conclude that whether such matrices were contaminated with ATZ, the use of GPC to remove the pollutant by adsorption would be efficient. Finally, the high efficiency observed for ATZ adsorption by GPC under all conditions analyzed in this study proves that its use as an adsorbent is a viable alternative for environmental remediation of ATZ-contaminated ecosystems. Also, desorption studies showed a potential application of this material for sample preparation processes aiming for ATZ analysis in environmental matrices. Such results were achieved due to thermodynamically favorable kinetic mechanism interactions between adsorbent and adsorbate. Fig. 7 showed a proposed mechanism for ATZ removal by adsorption on GPC, and its potential for ATZ environmental remediation was confirmed by comparison with other materials found in the literature (Table 5). The comparative data confirmed that the time required for GPC to promote efficient ATZ adsorption from the aqueous solution was up to 67% lower than that reported in the literature, proving its high efficiency. The q_m found for GPC was the highest among those compared in Table 5, confirming the high ATZ adsorption efficiency. Such results proved that the organized GPC structure obtained by the proposed synthesis method consists of well-distributed active sites on the surface of the material, thus achieving efficient pollutant adsorption.

4. Conclusion

The potential for removing the emerging contaminant ATZ from the aqueous solution using an efficient adsorbent (GPC) was investigated in this study. The graphitic-carbon-composed material with iron oxide sites showed a high surface area ($S_{BET} = 358$ m^2 g^{-1}) and significant porosity. As a catalytic graphitization by-product fostered by ferrocene, iron oxide denoted the dispersion of some magnetic domains in the material structure. Efficient ATZ removal (>95%) was achieved in time <20 min for a wide pH range (2–10) by applying a 500 mg L^{-1} dose of GPC in 20 mL of ATZ (15 mg L^{-1}) solution. The process sustainability was also proven by reuse studies for up to 4 application cycles, which may be expanded by adopting some simple procedures for adsorbent sites reactivation. As a complementary application, ATZ desorption was achieved in only 2 min using acetonitrile as extracting solvent. This result also highlighted the relevance of GPC potential for ATZ sample preparation processes based on solid phase extraction after the preconcentration stage. Kinetic and thermodynamic studies that fitted properly to the PSO (kinetic) and Langmuir (isotherms) model,

respectively, proved that surface interactions are crucial for ATZ removal. The calculated thermodynamic parameter (ΔG) showed that the adsorption process may reach an optimal q_e = 275.4 mg g^{-1}. Adsorption efficiency was reiterated when applying the materials to remove ATZ from natural water matrices, proving that GPC is a viable alternative for ATZ environmental remediation in aqueous media.

Credit author statement

Roberto Bertholdo: conceptualization and methodology. BET analysis. Carmen G. Renda and Cristiane de Oliveira: phenolic resin and graphitic porous carbon synthesis and characterization. Atrazine adsorption studies. Ailton J. Moreira e Ernesto C. Pereira: Kinetic and thermodynamic studies. Otavio A. P. Pereira: Revision of the kinetic data and statistical index calculations. Gian P. G. Freschi: reusability assays, All authors: discussions and conclusion.

Declaration of competing interest

The authors declare that they have no known competing financial interests or personal relationships that could have appeared to influence the work reported in this paper.

Data availability

Data will be made available on request.

Acknowledgments

The authors would like to thank the Fundação de Amparo à Pesquisa do Estado de Minas Gerais (FAPEMIG) for its financial support (Process number: 5.31/2021), the Coordenação de Aperfeiçoamento de Pessoal de Nível Superior (CAPES) and the Fundação de Amparo à Pesquisa do Estado de São Paulo (Grant numbers: 2013/07296–2, 2016/20609–8, and 2017/11986–5), the Conselho Nacional de Desenvolvimento Científico e Tecnológico (CNPq), Shell, and Finep (Agreements numbers: 00.13.0435.00 and 00.16.0033.00) for their support.

References

Achari, V.S., Lopez, R.M., Rajalakshmi, A.S., Jayasree, S., Shibin, O.M., John, D., Sekkar, V., 2021. Microporous carbon with highly dispersed nano-lanthanum oxide (La2O3) for enhanced adsorption of methylene blue. Separ. Purif. Technol. 279, 119626 https://doi.org/10.1016/j.seppur.2021.119626.

Ahsan, M.A., Jabbari, V., El-Gendy, A.A., Curry, M.L., Noveron, J.C., 2019. Ultrafast catalytic reduction of environmental pollutants in water via MOF-derived magnetic Ni and Cu nanoparticles encapsulated in porous carbon. Appl. Surf. Sci. 497, 143608 https://doi.org/10.1016/j.apsusc.2019.143608.

Alothman, Z.A., 2012. A review: fundamental aspects of silicate mesoporous materials. Materials 5, 2874–2902. https://doi.org/10.3390/ma5122874.

Anastopoulos, I., Pashalidis, I., Orfanos, A.G., Manariotis, I.D., Tatarchuk, T., Sellaoui, L., Bonilla-Petriciolet, A., Mittal, A., Núñez-Delgado, A., 2020. Removal of caffeine, nicotine and amoxicillin from (waste)waters by various adsorbents. A review. J. Environ. Manage. 261, 110236 https://doi.org/10.1016/j.jenvman.2020.110236.

Aquino, J.M., Miwa, D.W., Rodrigo, M.A., Motheo, A.J., 2017. Treatment of actual effluents produced in the manufacturing of atrazine by a photo-electrolytic process. Chemosphere. https://doi.org/10.1016/j.chemosphere.2016.12.154.

Barcellos, P., Araújo, T., Gomes, G., Bila, D., Canela, M.C., 2022. The fate of atrazine in tropical environments: photolysis, acute toxicity and endocrine disruptor potential. J. Braz. Chem. Soc. 33, 927–937. https://doi.org/10.21577/0103-5053.20220030.

Batista, L., Rabe, U., Altpeter, I., Hirsekorn, S., Dobmann, G., 2014. On the mechanism of nondestructive evaluation of cementite content in steels using a combination of magnetic Barkhausen noise and magnetic force microscopy techniques. J. Magn. Magn Mater. 354, 248–256. https://doi.org/10.1016/j.jmmm.2013.11.019.

Blázquez, G., Calero, M., Hernáinz, F., Tenorio, G., Martín-Lara, M.A., 2010. Equilibrium biosorption of lead(II) from aqueous solutions by solid waste from olive-oil production. Chem. Eng. J. 160, 615–622. https://doi.org/10.1016/j.cej.2010.03.085.

Brazil, 2005. Ministério do Meio Ambiente. Conselho Nacional de Meio Ambiente (CONAMA). Resolução N° 357 de 17 de março de 2005. http://www.mma.gov.br/port/conama/res/res05/res35705.pdf 2005.

Buarque, F.S., Lima, N.S., Soares, C.M.F., Marques, M.N., Cavalcanti, E.B., Pereira, M.M., Souza, R.L., Lima, Á.S., 2021. Preconcentration and chromatographic detection of atrazine in real water sample using aqueous two-phase system based on tetrahydrofuran and glycerol. Environ. Qual. Manag. 31, 39–48. https://doi.org/10.1002/tqem.21738.

Cao, Y., Jiang, S., Zhang, Y., Xu, J., Qiu, L., Wang, L., 2021. Investigation into adsorption characteristics and mechanism of atrazine on nano-MgO modified fallen leaf biochar. J. Environ. Chem. Eng. https://doi.org/10.1016/j.jece.2021.105727, 105727.

Cheng, Y., Wang, B., Shen, J., Yan, P., Kang, J., Wang, W., Bi, L., Zhu, X., Li, Y., Wang, S., Shen, L., Chen, Z., 2022. Preparation of novel N-doped biochar and its high adsorption capacity for atrazine based on π–π electron donor-acceptor interaction. J. Hazard Mater. 432 https://doi.org/10.1016/j.jhazmat.2022.128757.

Cougnaud, A., Faur, C., Le Cloirec, P., 2005. Removal of pesticides from aqueous solution: quantitative relationship between activated carbon characteristics and adsorption properties. Environ. Technol. 26, 857–866. https://doi.org/10.1080/09593332608618497.

European Commission, 2013. Herbicide Levels in Coastal Waters Drop after EU Ban _ Atrazine. https://doi.org/10.1016/j.marpolbul.20.

Freeman, L.E.B., Rusiecki, J.A., Hoppin, J.A., Lubin, J.H., Koutros, S., Andreotti, G., Zahm, S.H., Hines, C.J., Coble, J.B., Barone-Adesi, F., Sloan, J., Sandler, D.P., Blair, A., Alavanja, M.C.R., 2011. Atrazine and cancer incidence among pesticide applicators in the agricultural health study (1994–2007). Environ. Health Perspect. 119, 1253–1259. https://doi.org/10.1289/ehp.1103561.

Frikha, K., Limousy, L., Pons Claret, J., Vaulot, C., Pérez, K.F., Garcia, B.C., Bennici, S., 2022. Potential valorization of waste tires as activated carbon-based adsorbent for organic contaminants removal. Materials 15, 1099. https://doi.org/10.3390/ma15031099.

Gorito, A.M., Ribeiro, A.R., Almeida, C.M.R., Silva, A.M.T., 2017. A review on the application of constructed wetlands for the removal of priority substances and contaminants of emerging concern listed in recently launched EU legislation. Environ. Pollut. 227, 428–443. https://doi.org/10.1016/j.envpol.2017.04.060.

He, H., Liu, Y., You, S., Liu, J., Xiao, H., Tu, Z., 2019. A review on recent treatment technology for herbicide atrazine in contaminated environment. Int. J. Environ. Res. Publ. Health 16. https://doi.org/10.3390/ijerph16245129.

Hernandes, P.T., Franco, D.S.P., Georgin, J., Salau, N.P.G., Dotto, G.L., 2022. Adsorption of atrazine and 2,4-D pesticides on alternative biochars from cedar bark sawdust (Cedrella fissilis). Environ. Sci. Pollut. Res. 29, 22566–22575. https://doi.org/10.1007/s11356-021-17590-4.

Hong, K., Huang, Y., Zheng, L., Zheng, X., Huang, X., 2022. One-pot fabrication of poly (ionic liquid)s functionalized magnetic adsorbent for efficient enrichment of phenylurea herbicides in environmental waters. Anal. Chim. Acta 1198, 339549. https://doi.org/10.1016/j.aca.2022.339549.

Hu, Q., Zhang, Z., 2019. Application of Dubinin–Radushkevich isotherm model at the solid/solution interface: a theoretical analysis. J. Mol. Liq. 277, 646–648. https://doi.org/10.1016/j.molliq.2019.01.005.

Jaria, G., Calisto, V., Gil, M.V., Otero, M., Esteves, V.I., 2015. Removal of fluoxetine from water by adsorbent materials produced from paper mill sludge. J. Colloid Interface Sci. 448, 32–40. https://doi.org/10.1016/j.jcis.2015.02.002.

Jennings, A.A., Li, Z., 2017. Worldwide regulatory guidance values applied to direct contact surface soil pesticide contamination: Part I—carcinogenic pesticides. Air Soil. Water Res. 10, 117862211771193 https://doi.org/10.1177/1178622117711930.

Jia, D., Li, Yuejin, Li, Yaping, Li, C., 2013. Measurement and correlation of solubility of 2-Chloro-4-ethylamino-6-isopropylamino-1,3,5-triazine in different organic solvents. J. Chem. Eng. Data 58, 3183–3189. https://doi.org/10.1021/je400639m.

Jiao, W.-B., Zhang, Y.-Q., Yu, K., Zhou, J.-R., Cao, H.-L., Lü, J., 2019. Porous graphitic biomass carbons as sustainable adsorption and controlled release carriers for atrazine fixation. ACS Sustain. Chem. Eng. 7, 20180–20189. https://doi.org/10.1021/acssuschemeng.9b06269.

Júnior, O.G., Santos, M.G.B., Nossol, A.B.S., Starling, M.C.V.M., Trovó, A.G., 2021. Decontamination and toxicity removal of an industrial effluent containing pesticides via multistage treatment: coagulation-flocculation-settling and photo-Fenton process. Process Saf. Environ. Protect. 147, 674–683. https://doi.org/10.1016/j.psep.2020.12.021.

Karlsson, A.S., Lesch, M., Weihermüller, L., Thiele, B., Disko, U., Hofmann, D., Vereecken, H., Spielvogel, S., 2020. Pesticide contamination of the upper Elbe River and an adjacent floodplain area. J. Soils Sediments 20, 2067–2081. https://doi.org/10.1007/s11368-020-02571-w.

Król, M., Mozgawa, W., Jastrzębski, W., 2016. Theoretical and experimental study of ion-exchange process on zeolites from 5-1 structural group. J. Porous Mater. 23, 1–9. https://doi.org/10.1007/s10934-015-0050-6.

Lawtae, P., Tangsathitkulchai, C., 2021. The use of high surface area mesoporous-activated carbon from longan seed biomass for increasing capacity and kinetics of methylene blue adsorption from aqueous solution. Molecules 26, 6521. https://doi.org/10.3390/molecules26216521.

Lazarotto, J.S., da Boit Martinello, K., Georgin, J., Franco, D.S.P., Netto, M.S., Piccilli, D.G.A., Silva, L.F.O., Lima, E.C., Dotto, G.L., 2022. Application of araçá fruit husks (Psidium cattleianum) in the preparation of activated carbon with FeCl3 for atrazine herbicide adsorption. Chem. Eng. Res. Des. 180, 67–78. https://doi.org/10.1016/j.cherd.2022.01.044.

Li, H., Sadiq, M.M., Suzuki, K., Ricco, R., Doblin, C., Hill, A.J., Lim, S., Falcaro, P., Hill, M.R., 2016. Magnetic metal-organic frameworks for efficient carbon dioxide capture and remote trigger release. Adv. Mater. 28, 1839–1844. https://doi.org/10.1002/adma.201505320.

Li, H., Wang, F., Li, J., Deng, S., Zhang, S., 2021. Adsorption of three pesticides on polyethylene microplastics in aqueous solutions: kinetics, isotherms, thermodynamics, and molecular dynamics simulation. Chemosphere 264, 128556. https://doi.org/10.1016/j.chemosphere.2020.128556.

Li, Z.Q., Lu, C.J., Xia, Z.P., Zhou, Y., Luo, Z., 2007. X-ray diffraction patterns of graphite and turbostratic carbon. Carbon N. Y. 45, 1686–1695. https://doi.org/10.1016/j.carbon.2007.03.038.

Lima, E.C., Hosseini-Bandegharaei, A., Moreno-Pirajᵃn, J.C., Anastopoulos, I., 2019. A critical review of the estimation of the thermodynamic parameters on adsorption equilibria. Wrong use of equilibrium constant in the Van't Hoof equation for calculation of thermodynamic parameters of adsorption. J. Mol. Liq. 273, 425–434. https://doi.org/10.1016/j.molliq.2018.10.048.

Lv, Z., Wang, H., Chen, C., Yang, S., Chen, L., Alsaedi, A., Hayat, T., 2019. Enhanced removal of uranium(VI) from aqueous solution by a novel Mg-MOF-74-derived porous MgO/carbon adsorbent. J. Colloid Interface Sci. 537, A1–A10. https://doi.org/10.1016/j.jcis.2018.11.062.

Mandal, A., Kumar, A., Singh, N., 2021. Sorption mechanisms of pesticides removal from effluent matrix using biochar: conclusions from molecular modelling studies validated by single-, binary and ternary solute experiments. J. Environ. Manag. 295, 113104 https://doi.org/10.1016/j.jenvman.2021.113104.

Mandal, A., Singh, N., Purakayastha, T.J., 2017. Characterization of pesticide sorption behaviour of slow pyrolysis biochars as low cost adsorbent for atrazine and imidacloprid removal. Sci. Total Environ. 577, 376–385. https://doi.org/10.1016/j.scitotenv.2016.10.204.

Mohammadzadeh, A., Kadhim, M.M., Taban, T.Z., Baigenzhenov, O., Ivanets, A., Lal, B., Kumar, N., Hosseini-Bandegharaei, A., 2022. Adsorption performance of Enterobacter cloacae towards U(VI) ion and application of Enterobacter cloacae/carbon nanotubes to preconcentration and determination of low-levels of U(VI) in water samples. Chemosphere 311, 136804. https://doi.org/10.1016/j.chemosphere.2022.136804.

Moreira, A.J., Coelho, D., Dias, J.A., Mascaro, L.H., Freschi, G.P.G., Mastelaro, V.R., Pereira, E.C., 2022. Phase control and optimization of photocatalytical properties of samarium doped TiO2 synthesized by coupled ultraviolet and microwave radiations. J. Alloys Compd. 905, 164217 https://doi.org/10.1016/j.jallcom.2022.164217.

Moreira, A.J., Lemos, S.G., Coelho, D., Mascaro, L.H., Freschi, G.P.G., Pereira, E.C., 2021. UV–Vis spectrophotometry coupled to chemometric analysis for the performance evaluation of atrazine photolysis and photocatalysis. Environ. Sci. Pollut. Res. https://doi.org/10.1007/s11356-021-17687-w.

Naushad, M., Alqadami, A.A., Al-Kahtani, A.A., Ahamad, T., Awual, M.R., Tatarchuk, T., 2019. Adsorption of textile dye using para-aminobenzoic acid modified activated carbon: kinetic and equilibrium studies. J. Mol. Liq. 296, 112075 https://doi.org/10.1016/j.molliq.2019.112075.

Paris, E.C., Malafatti, J.O.D., Moreira, A.J., Santos, L.C., Sciena, C.R., Zenatti, A., Escote, M.T., Mastelaro, V.R., Joya, M.R., 2022. CuO nanoparticles decorated on hydroxyapatite/ferrite magnetic support: photocatalysis, cytotoxicity, and antimicrobial response. Environ. Sci. Pollut. Res. 29, 41505–41519. https://doi.org/10.1007/s11356-021-18263-y.

Peiravi-Rivash, O., Mashreghi, M., Baigenzhenov, O., Hosseini-Bandegharaei, A., 2022. Producing bacterial nano-cellulose and keratin from wastes to synthesize keratin/cellulose nanobiocomposite for removal of dyes and heavy metal ions from waters and wastewaters. Colloids Surfaces A Physicochem. Eng. Asp. 656, 130355 https://doi.org/10.1016/j.colsurfa.2022.130355.

Pelekani, C., Snoeyink, V.L., 2001. A kinetic and equilibrium study of competitive adsorption between atrazine and Congo red dye on activated carbon: the importance of pore size distribution. Carbon N. Y. 39, 25–37. https://doi.org/10.1016/S0008-6223(00)00078-6.

Pinson, M.B., Zhou, T., Jennings, H.M., Bazant, M.Z., 2018. Inferring pore connectivity from sorption hysteresis in multiscale porous media. J. Colloid Interface Sci. 532, 118–127. https://doi.org/10.1016/j.jcis.2018.07.095.

Rahmani-Sani, A., Singh, P., Raizada, P., Claudio Lima, E., Anastopoulos, I., Giannakoudakis, D.A., Sivamani, S., Dontsova, T.A., Hosseini-Bandegharaei, A., 2020. Use of chicken feather and eggshell to synthesize a novel magnetized activated carbon for sorption of heavy metal ions. Bioresour. Technol. 297, 122452 https://doi.org/10.1016/j.biortech.2019.122452.

Regalbuto, J.R., Robles, J.O., 2004. The Engineering of Pt/Carbon Catalyst Preparation. Univ. Illinois, Chicago, p. 13.

Renda, C.G., Bertholdo, R., 2018. Study of phenolic resin and their tendency for carbon graphitization. J. Polym. Res. 25, 241. https://doi.org/10.1007/s10965-018-1635-y.

Renda, C.G., Bertholdo, R., Venâncio, T., Luz, A.P., Pandolfelli, V.C., Lucas, A.A., 2019. Influence of the mixing process on the graphitization of phenolic resins. Ceram. Int. 45, 12196–12204. https://doi.org/10.1016/j.ceramint.2019.03.124.

Renda, C.G., Contreras Medrano, C.P., Costa, L.J.D., Litterst, F.J., Saitovitch, E.M.B., Magon, C.J., Gualdi, A.J., Venâncio, T., Bertholdo, R., Moreira, A.J., Freschi, G.P.G., de Almeida Lucas, A., 2021a. Role of ferrocene-derived iron species in the catalytic graphitization of novolak resins. J. Mater. Sci. 56, 1298–1311. https://doi.org/10.1007/s10853-020-05312-z.

Renda, C.G., Goulart, L.A., Fernandes, C.H.M., Mascaro, L.H., de Aquino, J.M., Bertholdo, R., 2021b. Novel onion-like carbon structures modified with iron oxide as photocatalysts for the degradation of persistent pollutants. J. Environ. Chem. Eng. 9, 104934 https://doi.org/10.1016/j.jece.2020.104934.

Ryberg, K.R., Stone, W.W., Baker, N.T., 2020. Causal factors for pesticide trends in streams of the United States: atrazine and deethylatrazine. J. Environ. Qual. 49, 152–162. https://doi.org/10.1002/jeq2.20045.

Saeed, A.M., Wisner, C.A., Donthula, S., Majedi Far, H., Sotiriou-Leventis, C., Leventis, N., 2016. Reuseable monolithic nanoporous graphite-supported nanocatalysts (Fe, Au, Pt, Pd, Ni, and Rh) from pyrolysis and galvanic transmetalation of ferrocene-based polyamide aerogels. Chem. Mater. 28, 4867–4877. https://doi.org/10.1021/acs.chemmater.6b02364.

Salomón, Y.L., Georgin, J., Franco, D.S.P., Netto, M.S., Piccilli, D.G.A., Foletto, E.L., Pinto, D., Oliveira, M.L.S., Dotto, G.L., 2022. Adsorption of atrazine herbicide from water by diospyros kaki fruit waste activated carbon. J. Mol. Liq. 347, 117990 https://doi.org/10.1016/j.molliq.2021.117990.

Saxena, N., Kumar, A., Mandal, A., 2019. Adsorption analysis of natural anionic surfactant for enhanced oil recovery: the role of mineralogy, salinity, alkalinity and nanoparticles. J. Pet. Sci. Eng. 173, 1264–1283. https://doi.org/10.1016/j.petrol.2018.11.002.

Sbizzaro, M., César Sampaio, S., Rinaldo dos Reis, R., de Assis Beraldi, F., Medina Rosa, D., Maria Branco de Freitas Maia, C., Saramago de Carvalho Marques dos Santos Cordovil, C., Tillvitz do Nascimento, C., Antonio da Silva, E., Eduardo Borba, C., 2021. Effect of production temperature in biochar properties from bamboo culm and its influences on atrazine adsorption from aqueous systems. J. Mol. Liq. 343, 117667 https://doi.org/10.1016/j.molliq.2021.117667.

Seibel, C., Wedler, C., Vorobiev, N., Schiemann, M., Scherer, V., Span, R., Fieback, T.M., 2016. Sorption measurements for determining surface effects and structure of solid fuels. Fuel Process. Technol. 153, 81–86. https://doi.org/10.1016/j.fuproc.2016.08.004.

Singh, S., Kumar, V., Chauhan, A., Datta, S., Wani, A.B., Singh, N., Singh, J., 2018. Toxicity, degradation and analysis of the herbicide atrazine. Environ. Chem. Lett. 16, 211–237. https://doi.org/10.1007/s10311-017-0665-8.

Stackpoole, S.M., Shoda, M.E., Medalie, L., Stone, W.W., 2021. Pesticides in US Rivers: regional differences in use, occurrence, and environmental toxicity, 2013 to 2017. Sci. Total Environ. 787, 147147 https://doi.org/10.1016/j.scitotenv.2021.147147.

Sun, Q., Yang, L., 2003. The adsorption of basic dyes from aqueous solution on modified peat–resin particle. Water Res. 37, 1535–1544. https://doi.org/10.1016/S0043-1354(02)00520-1.

Švorc, Ľ., Rievaj, M., Bustin, D., 2013. Green electrochemical sensor for environmental monitoring of pesticides: determination of atrazine in river waters using a boron-doped diamond electrode. Sens. Actuators, B 181, 294–300. https://doi.org/10.1016/j.snb.2013.02.036.

Tran, H.N., You, S.-J.J., Hosseini-Bandegharaei, A., Chao, H.-P.P., 2017. Mistakes and inconsistencies regarding adsorption of contaminants from aqueous solutions: a critical review. Water Res. 120, 88–116. https://doi.org/10.1016/j.watres.2017.04.014.

Vargas, A.M.M., Cazetta, A.L., Kunita, M.H., Silva, T.L., Almeida, V.C., 2011. Adsorption of methylene blue on activated carbon produced from flamboyant pods (Delonix regia): study of adsorption isotherms and kinetic models. Chem. Eng. J. 168, 722–730. https://doi.org/10.1016/j.cej.2011.01.067.

Varsha, M., Senthil Kumar, P., Senthil Rathi, B., 2022. A review on recent trends in the removal of emerging contaminants from aquatic environment using low-cost adsorbents. Chemosphere 287, 132270. https://doi.org/10.1016/j.chemosphere.2021.132270.

Wang, Y., Liu, C., Wang, F., Sun, Q., 2022. Behavior and mechanism of atrazine adsorption on pristine and aged microplastics in the aquatic environment: kinetic and thermodynamic studies. Chemosphere 292, 133425. https://doi.org/10.1016/j.chemosphere.2021.133425.

Wu, F.-C., Tseng, R.-L., Juang, R.-S., 2009. Initial behavior of intraparticle diffusion model used in the description of adsorption kinetics. Chem. Eng. J. 153, 1–8. https://doi.org/10.1016/j.cej.2009.04.042.

Yang, F., Sun, L., Xie, W., Jiang, Q., Gao, Y., Zhang, W., Zhang, Y., 2017. Nitrogen-functionalization biochars derived from wheat straws via molten salt synthesis: an efficient adsorbent for atrazine removal. Sci. Total Environ. 607–608, 1391–1399. https://doi.org/10.1016/j.scitotenv.2017.07.020.

Zhu, B., Xia, P., Ho, W., Yu, J., 2015. Isoelectric point and adsorption activity of porous g-C3N4. Appl. Surf. Sci. 344, 188–195. https://doi.org/10.1016/j.apsusc.2015.03.086.

Zielińska-Jurek, A., Bielan, Z., Dudziak, S., Wolak, I., Sobczak, Z., Klimczuk, T., Nowaczyk, G., Hupka, J., 2017. Design and application of magnetic photocatalysts for water treatment. The effect of particle charge on surface functionality. Catalysts 7. https://doi.org/10.3390/catal7120360.